Revisiting Protein Protected Gold and Silver Nanoclusters: Excited State Dynamics and Long-Lived Emission

Shagun Sharma[a], Subhadeep Das[b], Kush Kaushik[a], Abhijit Patra[b] Chayan Kanti Nandi[a]*

[a]*School of Chemical Sciences, Indian Institute of Technology (IIT) Mandi, H.P- 175075*

[b]*Department of Chemistry, Indian Institute of Science Education and Research (IISER) Bhopal, M.P-462066*

Abstract

Owing to their intriguing photophysical properties, protein-functionalized metal nanoclusters (MNCs) have become benchmark nanomaterials in various fields including electronics, optics, energy, sensing, and biomedicine. However, the excited state dynamics of these MNCs, especially the long-lived emission, remain a debatable topic. Here, we investigated the excited-state dynamics of bovine serum albumin (BSA) functionalized Ag and Au nanoclusters (BSA-Ag NCs and BSA-Au NCs) and provided new insights into their long-lived emission. Our results showed completely different excited state dynamics in these MNCs despite their closely similar number of atoms in the BSA-caged metal core. BSA-Au NCs showed short-lived emission followed by a long-lived excited state at room temperature, originating from the core and surface states, respectively. In contrast, the BSA-Ag NCs showed short-lived emission originating only from the core states. The long-lived emission of BSA-Au NCs was attributed to ligand-to-metal charge transfer (LMCT) facilitated by the presence of strong metal-sulfur (M-S) bonds. The time-resolved luminescence imaging (TRLI) microscopy of both MNCs in HeLa cells indeed confirmed the long-lived emission characteristics in BSA-Au NCs but not in BSA-Ag NCs.

Keywords: Nanoclusters, Bovine serum albumin, long-lived emission, Room temperature phosphorescence, Time-resolved luminescence imaging, TRANES

The metal nanoclusters (MNCs) have witnessed significant progress in recent years owing to their intriguing photophysical properties such as near-infrared emission, large Stokes shift, low cytotoxicity, and long photoluminescence lifetimes.[1–4] Among various ligand-protected MNCs, protein-functionalized MNCs are particularly interesting because of their facile synthesis, low toxicity and excellent biocompatibility.[5–8] This makes them highly versatile for application in multidisciplinary fields, including electronics, optics, energy, sensing, and biomedicine.[9–11] However, the excited state dynamics of these protein-functionalized MNCs remain a debatable topic, largely due to the presence of multiple emissive centers within the nanoclusters.[12,13]

Structurally, protein surface functionalized MNCs consist of tens of metal atoms encapsulated within the protein cages or binding units, which prevent it from aggregation and provide structural stability.[5,14,15] The metal atoms are typically linked to the protein layer via the sulphur atom of the cysteine residue of the protein (**Figure 1a**).[8] Since the discovery of the biomineralization approach for the synthesis of bovine serum albumin (BSA) protected gold and silver nanoclusters, there has been a growing number of studies on these clusters.[6,16–20] Time-resolved luminescence studies have been employed to elucidate the deexcitation mechanism of the photoluminescence in these MNCs.[21,22] Considering the decay characteristics, it is proposed that the nanosecond lifetime mainly originates from the metal-metal (M-M) core emission of the MNCs. A lifetime of sub-microseconds ranging from 100-200 ns is associated with the emission from the ligand to metal charge transfer (LMCT) states, originating from the intramolecular interactions involving metal core and surface motifs.[23] Most importantly, the long-lived lifetime from microseconds to milliseconds results from the thermally activated delayed fluorescence (TADF) or room temperature phosphorescence (RTP) (**Figure 1a**).[24–26]

The Jablonski diagram presented in **Figure 1b** depicts the above three types of deexcitation mechanisms encountered in MNCs. The fluorescence emission is observed when the electron relaxation occurs from the excited singlet state. The emission has also been occurring from the electronic transition from LMCT states. These LMCT states arise from the metalophillic (M(I)–M(I)) interactions and the charge transfer between the metal core and surface motifs.[27,28] Both TADF and RTP mechanisms involve triplet state harvesting, with a distinct difference in the emission pathways. For TADF emitters, long-lived emission arises from the excited singlet state following the reverse intersystem crossing (RISC) from the triplet state, whereas RTP involves deexcitation directly from the triplet state. The dominance of the TADF or RTP

depends on the rates of intersystem crossing (K_{ISC}), rate of phosphorescence (K_{Ph}) and the rate of reverse intersystem crossing (K_{rISC}).[29,30]

Considering the massive size of BSA, with many electron donors, all the BSA nanoclusters with nearly similar numbers of core metal atoms are expected to exhibit similar excited state photophysical properties. Indeed, the reported emission spectra originating in the BSA functionalized Au and Ag nanoclusters showed similar type of emission spectra in the red region with a peak maximum spanning from 650 to 670 nm (**Figure 1c**). Here, we aim to revisit the excited-state dynamics of BSA-protected Ag and Au nanoclusters (BSA-Au NCs and BSA-Ag NCs) and to provide new insights into these well-studied MNCs through comprehensive and systematic investigation. We show completely different excited state dynamics, especially the long-lived emission characteristics in these MNCs. While BSA-Au NCs showed a short-lived excited state followed by a long-lived emission originating from the core and surface states, the BSA-Ag NCs showed predominant short-lived emission, involving the core states. The strong interaction between the metal core and surface motifs via the M-S bond supports LMCT states in BSA-Au NCs, whereas such interactions are weak in BSA-Ag NCs. The time-resolved emission spectra (TRES), the time-resolved area normalization emission spectra (TRANES) and the temperature-dependent luminescence measurements confirmed the RTP mechanism in BSA-Au NCs for the long-lived emission. In contrast, BSA-Ag NCs exhibit only fluorescence as the deexcitation mechanism at room temperature (RT). However, it is transitioned to phosphorescence at 77 K which is due to the suppressed solvent and vibrational relaxations in a rigid environment. The time-resolved luminescence imaging (TRLI) microscopy of both MNCs in HeLa cells indeed confirmed the long-lived emission characteristics in BSA-Au NCs but not in BSA-Ag NCs.

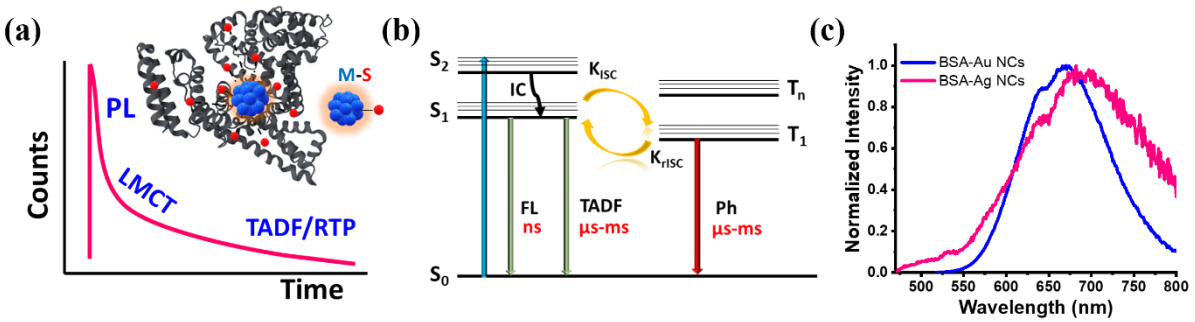

Figure 1. (a) Schematic representation of the possible structure and the typical lifetime decay curve of protein-conjugated MNCs. (b) The energy level diagram illustrating the mechanisms for the varied lifetime range, helped in understanding the excited state dynamics of (c) red-emissive BSA-Ag NCs and BSA-Au NCs.

The synthesis of BSA-Ag NCs and BSA-Au NCs was carried out by the previously reported protocol.[31,32] The transmission electron microscopy (TEM) data of about 100 particles suggested that BSA-Ag NCs and BSA-Au NCs have closely similar diameters of 3.0 nm and 3.1 nm, respectively (**Figure S1a and S2a**). This was further well corroborated with the hydrodynamic diameter of the nanoclusters calculated using fluorescence correlation spectroscopy (FCS, **Figure S1b, S2b** details in supporting information SI). The parameters obtained from the fitting analysis, namely diffusion times (τ_D), diffusion coefficient (D_t), number of molecules (N), hydrodynamic radius (r_h), and diameter of the BSA-Ag NCs and BSA-Au NCs are presented in **Table S1 and Table S2 respectively**. The matrix-assisted laser desorption/ionization-time of flight (MALDI-TOF) mass spectrometry data showed that BSA-Ag NCs consist of 30 Ag atoms (**Figure S3**). The number of Au atoms in BSA-Au NCs is 25, corroborated by the reported literature.[31,33,34] The XPS spectra of Ag 3d provide two distinct components. The peaks with binding energy (BE) of 368.2 eV (Ag $3d_{5/2}$) and 374.2 eV (Ag $3d_{3/2}$) are designated for Ag (0), and 368.8 eV (Ag $3d_{5/2}$) and 374.8 eV (Ag $3d_{3/2}$) are assigned

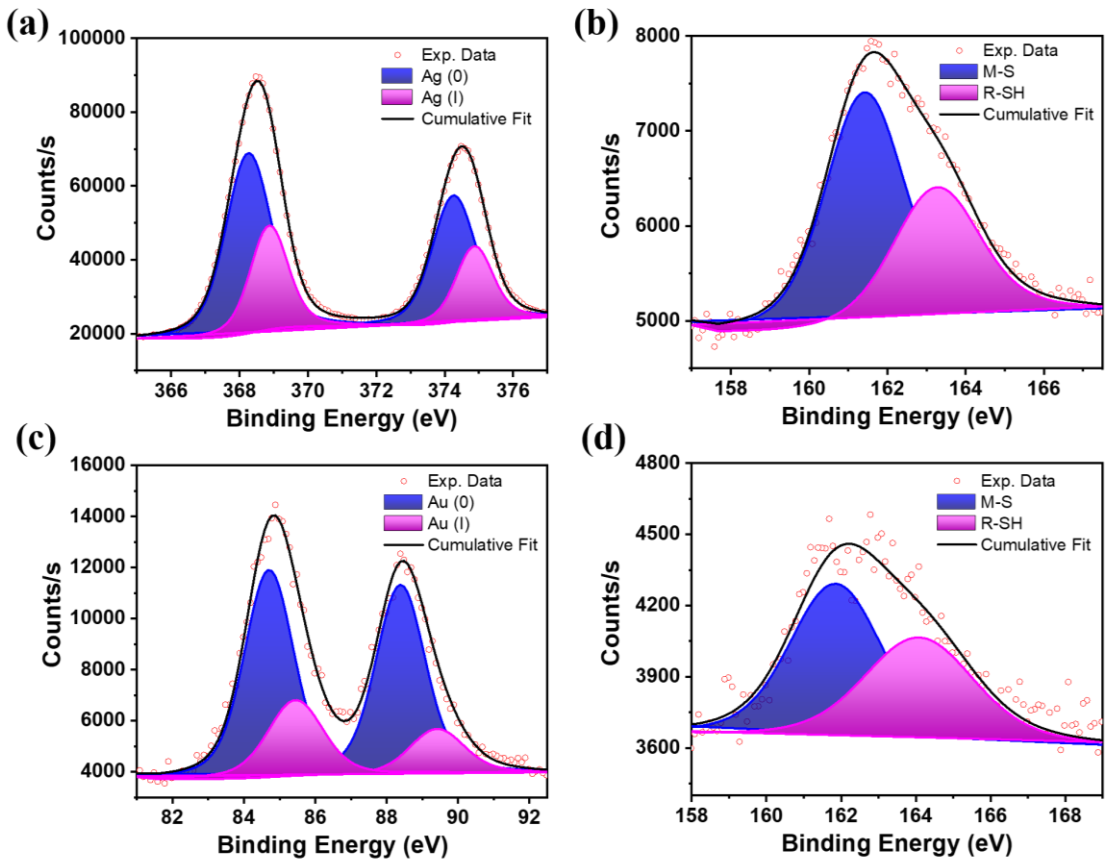

Figure 2. Deconvoluted X-ray photoelectron spectroscopy (XPS) profiles of (a) Ag 3d scan and (b) S 2p scan of BSA-Ag NCs. (c) Au 4f scan and (d) S 2p scan of BSA-Au NCs after etching time of 540.783 s.

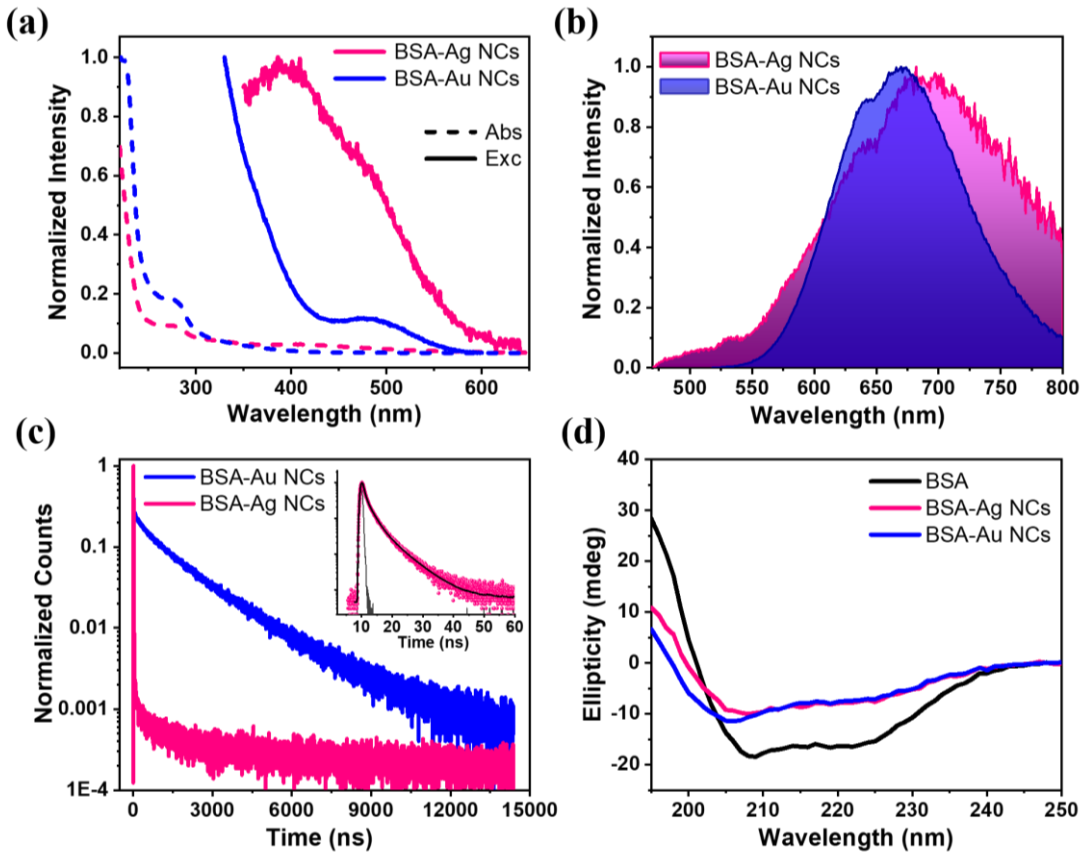

Figure 3. (a) The absorption, excitation and (b) the emission spectra of BSA-Ag NCs and BSA-Au NCs. (c) The lifetime decay curve of BSA-Ag NCs and BSA-Au NCs using measurement range of 13 µs, inset: the lifetime decay curve of BSA-Ag NCs using measurement range of 100 ns. (d) The CD spectra of native BSA, BSA-Ag NCs and BSA-Au NCs all at the concentration of 0.1 mg mL^{-1}.

for Ag (I).[35] The contributions of Ag (0) and Ag (I) were 67% and 33%, respectively (**Figure 2a**). These results indicate that the core of the BSA-Ag NCs is stabilized both by zerovalent and univalent silver atoms. The peak at 161.4 eV in the high-resolution deconvolution data of S2p of BSA-Ag NCs (**Figure 2b**) is assigned to the metal-sulphur bond and the peak at 163.4 eV signified the unbound S of the BSA ligand.[36] The XPS data of BSA-Au NCs showed two peaks at 84.8 eV and 88.4 eV, which were attributed to $4f_{7/2}$ and $4f_{5/2}$ for Au respectively (**Figure 2c**) The former peak was further deconvoluted into two distinct components at 84.6 eV and 85.4 eV which were assigned to Au (0) (75%) and Au (I) (25%) respectively.[19] The S2p XPS spectrum of BSA-Au NCs shows two broad peaks at 161.8 eV and 164 eV, which is ascribed to sulphur bound to gold and the unbound sulphur of BSA, respectively (**Figure 2d**).[37] It is important to note that the similar percentages of Ag (0) and Au (0) suggest a resemblance in the metallic core structure, while the similar percentages of Ag (I) and Au (I) indicate similarities in the surface ligand structure of both MNCs.

To understand the optical properties of BSA-Au NCs and BSA-Ag NCs, UV−vis absorption, excitation, and emission spectra were recorded. The absorption spectra of both the MNCs showed broad featureless absorption with a peak maximum at 280 nm, corresponding to the absorption originating from the tryptophan residues in BSA (**Figure 3a**).[38] The emission spectra in both cases showed a red emission with a peak maxima at around 670 nm for BSA-Au NCs and 680 nm for BSA-Ag NCs when excited at 450 nm (**Figure 3b**). Surprisingly, the excitation spectra of both the MNCs are distinctly different (**Figure 3a**). The BSA-Ag NCs show broad excitation with the excitation maximum at 400 nm, whereas the BSA-Au NCs showed progressively decreased excitation spectra with a hump at around 490 nm. This suggests that the different excited states are responsible for the emission in respective nanoclusters. The above results prompted us to understand the detailed mechanism and pathways of the excited state dynamics in both MNCs.

To investigate the excited state behaviour of red emissive MNCs, we employed luminescence lifetime measurements. BSA-Ag NCs showed the nanosecond lifetime as the dominant lifetime (**inset of Figure 3c**). The average lifetime of BSA-Ag NCs is 2.3 ns. The individual lifetime components with their amplitudes are presented in **Table 1**. Additionally, a negligibly small sub-microsecond component is observed from the decay curve of BSA-Ag NCs presented in **Figure 3c**. The short and long lifetimes presented in the lifetime decay curve are tail-fitted separately (**Figure S4**) with the fitting parameters mentioned in **Table S3**. On the contrary, the BSA-Au NCs showed a microsecond lifetime as the dominant one (**Figure 3c**). The average lifetime of BSA-Au NCs is found to be ~1 μs (0.97 μs) using the triexponential function for fitting (**Table 1**). The fraction of microsecond lifetime (A_3) is much more in comparison to the nanosecond lifetime (A_1) in BSA-Au NCs. This distinct variation in the excited state lifetime in the MNCs led us to think if any conformational or secondary structural changes occurred in BSA during the MNCs formation. Hence, we performed circular dichroism (CD) measurements of the BSA and BSA conjugated MNCs. Typically, BSA showed two peaks in

Table 1. Represents the lifetime (ns) fitting parameters of BSA-Ag NCs and BSA-Au NCs including individual lifetime components with their amplitudes.

S. No.	τ_1	τ_2	τ_3	A_1	A_2	A_3	τ_{av}
BSA-Ag NCs	1.8	0.4	6.1	41.4	34.4	24.0	2.3
BSA-Au NCs	80	579	1700	20.8	34.6	44.4	972

the CD spectrum at 209 nm and 222 nm, which are the characteristics of the α-helical secondary structure of native BSA.[39] The data presented in **Figure 3d** showed an obvious change in the helical structure when both the BSA-MNCs were formed. However, the change in ellipticity was similar in extent for both types of BSA-MNCs. We calculated the ellipticity percentage changes for BSA and BSA conjugated MNCs.[40] For instance, the alpha helicity in BSA is 56.5 %, while it is found to be 25.1 % and 21.4 % for BSA-Au NCs and BSA-Ag NCs, respectively. This suggests similar conformational changes in BSA during the nanocluster formation for both BSA-MNCs.[41]

The observed results ruled out the conformational or secondary structural changes, responsible for the distinct excited state lifetimes in BSA-MNCs. Therefore, to further understand the differences in their excited state decay profile at RT, TRES was employed to elucidate the distribution of the emissive states that evolved with time.[42] For the TRES acquisition of BSA-Ag NCs, an excitation wavelength of 454 nm was used (details of the TRES acquisition are provided in SI). **Figure 4a** displays the TRES of BSA-Ag NCs, which shows the evolution of the emission spectra over the nanosecond timescale (at certain time delays). The data showed spectral migration from 600 nm to 630 nm with the time evolution from 0.78 ns to 6.5 ns. The TRES data aligned well with the time-resolved area normalized spectra (TRANES) showing similar spectral shifting (**Figure 4b)**. This spectral shifting seen in the TRES and TRANES of BSA-Ag NCs might be from the heterogeneity of the excited states arising due to intermolecular solvent relaxation.[43] To get more information, TRES and TRANES were also recorded at 389 nm excitation, where no such spectral migration was seen, and the emission originated from a single state (**Figure 4c and 4d**). Like BSA-Ag NCs, the TRES and TRANES of BSA-Au NCs were also recorded at 454 nm and 389 nm excitation. A distinct excited state dynamics was observed. The TRES data recorded at 454 nm excitation revealed the presence of two excited states responsible for emission in BSA-Au NCs. However, the spectral information of the short-lived state was inconclusive (**Figure 4e**). The TRANES plotted for the TRES also failed to provide complete details about the short-lived state, despite the presence of an iso-emissive point shown in **Figure 4f**. To fully characterize both the emissive states involved in the deexcitation, TRES was acquired at 389 nm excitation. The data illustrate that the short nanosecond lifetime originates from the singlet state at 450 nm, while the long-lifetime emission is associated with the triplet state at 650 nm (**Figure 4g**). The short-lived emissive state exists for 54 ns, after which the long-lived state dominates. Also, the iso-

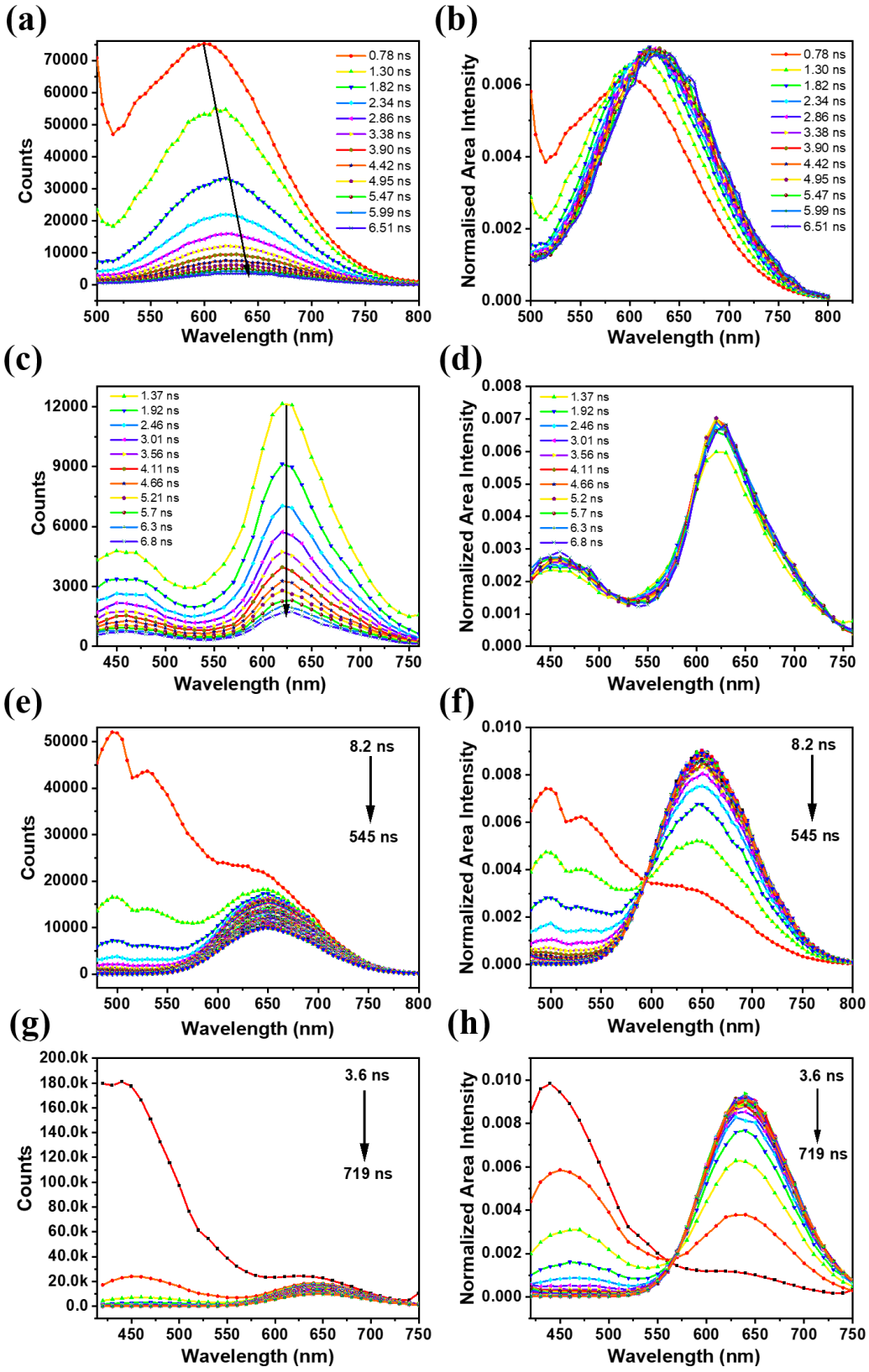

Figure 4. (a, c) The TRES and the (b, d) TRANES of BSA-Ag NCs [(a, b) - λ_{ex} = 454 nm; (c, d) - λ_{ex} = 389 nm (measurement range 100 ns)]. (e, g) The TRES and the (f, h) TRANES of BSA-Au NCs [(e, f) - λ_{ex} = 454 nm; (g, h) - λ_{ex} = 389 nm (measurement range 800 ns)].

170 emissive point in the TRANES spectra suggested that BSA-Au NCs showed dual emission

(**Figure 4h**).

Summarizing the above observations, both BSA-MNCs displayed heterogeneity in their excited states. However, the origin of such heterogeneity is different in both the nanoclusters. The TRES and TRANES studies of BSA-MNCs indicated that the high energy excitation (389 nm) is attributed to the core state excitation, while low energy excitation (454 nm) was associated with surface state excitation.[44] For instance, the TRES data acquired at 454 nm, failed to provide the core state information for BSA-Au NCs, whereas at 389 nm excitation, spectral information of both the short and long-lived emissive states could be achieved. For BSA-Ag NCs, as there is a lack of core and surface state interactions, only the core state emission was found at 389 nm excitation. The spectral shifting due to solvent-induced intermolecular interactions, occurring only at the surface motifs, was observed at 454 nm excitation.

The difference in the core and surface state interaction might arise due to the variations in the charge transfer from the surface ligands to the metal core via the sulphur-metal bond, influenced by the specific metal involved in the interaction. The role of charge transfer states in the emission of BSA-conjugated Au and Ag nanoclusters was demonstrated by observing the change in the emission in both clusters using a well-known electron accepter methyl viologen (MV). To this endeavour, BSA-MNCs were incubated with the 1 mM solution of MV. To our surprise, a complete quenching of fluorescence intensity was observed from steady-state luminescence spectra of BSA-Au NCs, while the fluorescence intensity is unchanged with the addition of MV in BSA-Ag NCs (**Figure S5a and S5b).** This result indicated that MV aids the formation of the dark state by decreasing the potential energy barrier of the electron transfer process in BSA-Au NCs. Also, the charge transfer states formed due to electron donation via the S-metal bond have been quenched by the involvement of electron acceptor MV. This is due to the electron donation from the N and O-rich groups in the BSA ligand to MV.[45] The complete quenching of fluorescence intensity is supposed to be due to the disruption of charge transfer states which is responsible for the origin of phosphorescence in BSA-Au NCs.

To gain greater details about the ambiguous results in both the MNCs, the stability of the BSA-MNCs is understood by observing the changes in their chemical composition with aging, through XPS analysis. For that, both the as-synthesized and aged BSA-MNCs (1 week old) were subjected to XPS analysis. As evident from **Figure S6 and Table S4,** the contribution of Ag (0) and Ag (I) within the BSA-Ag NCs, has changed from the as synthesized sample to the

aged sample (1 week old). Owning to the oxidation, the Ag (0) percentage decreased from 67 % to 25 %, whereas the binding energies remained the same. The results highlight the intrinsic instability of BSA-Ag nanoclusters, which influences the harvesting of triplet states in the clusters. In contrast, when a similar analysis was performed on BSA-Au NCs, no significant changes in chemical composition were observed with aging; the contribution of Au (0) and Au (I) remained consistent (**Figure S6 and Table S5**).

For a deeper understanding of the triplet state dynamics, phosphorescence measurements of BSA-Ag NCs were done in cryogenic conditions. The phosphorescence spectrum was measured at 77 K, with a time delay of 100 µs such that all the contributions from the fluorescence and scatterings could be eliminated. **Figure 5a** represents the normalized plot of fluorescence at room temperature (RT) and phosphorescence spectra at 77 K. It is believed that the emission is originating from the triplet state, which can be visualized from the red shift in the phosphorescence spectra of BSA-Ag NCs. Additionally, as we move from RT to 77 K, the spectral broadening decreases. This reduction may be due to rigidity induced at low temperatures, which restricts solvent-induced intermolecular interactions, which are the main cause for triplet state instability at RT. Due to the rigidity induced at 77 K, the lifetime decay curve of BSA-Ag NCs showed a sub-millisecond lifetime (**Figure 5c**).

We also unveiled the relaxation pathway of the long-lived emission in BSA-Au nanoclusters. For that, BSA-Au NCs is analyzed using TRES, temperature-dependent steady-state measurements, and time-resolved luminescence studies, with a focus on the delayed part of emission. As the long-lived emission (microsecond) is dominating in BSA-Au NCs, a time delay of 1 µs is chosen for the temperature-dependent measurements. The emission intensity

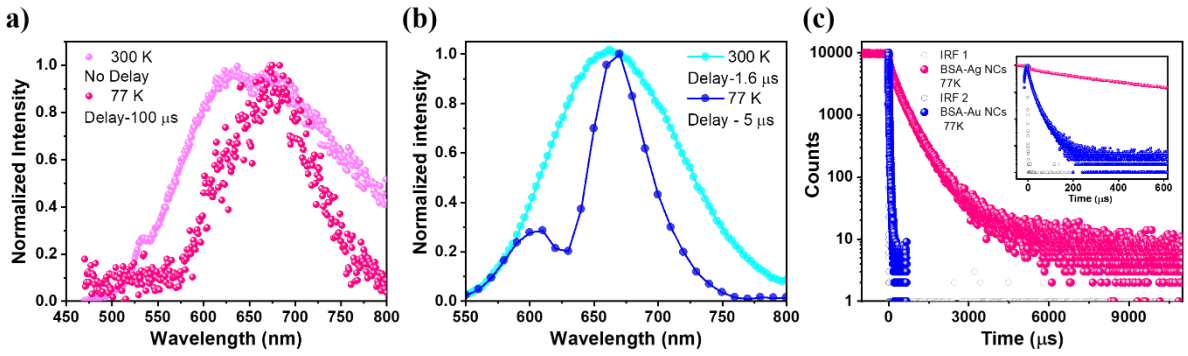

Figure 5. (a) Normalized emission spectra of BSA-Ag NCs recorded under ambient conditions (T = 298 K, λ_{ex} = 454 nm, no time delay) and 77 K (λ_{ex} = 454 nm, delay of 100 µs), respectively. (b) Time-resolved emission spectra (TRES) profiles of BSA-Au NCs at 300 K (time delay: 1.6 µs) and 77 K (time delay: 5.0 µs). (λ_{ex} = 417 nm, λ_{em} = 660 nm). (c) The lifetime decay profile of BSA-Ag NCs (τ_{av} = 0.48 ms) and BSA-Au NCs (τ_{av} = 18 µs) at 77 K; inset shows the zoomed view of the decay curves.

decreases with the increase in temperature from 283 K to 323 K (**Figure S7a)**. As the rISC become prominent at high temperatures, the decrement in the intensity rules out the TADF process in BSA-Au NCs. To support this observation, the lifetime measurements were performed, which showed the obvious decrement in the lifetime values with the increment in the temperature from 283 K to 323 K (**Figure S7b**). The temperature-dependent measurements exclude the possibility of the TADF mechanism in BSA-Au NCs. Similarly, TRANES data, which distinguish the long-lived emissive state from the short-lived state, further rule out the possibility of a TADF pathway for deexcitation. This suggests that room-temperature phosphorescence is likely the dominant pathway for emission in BSA-Au NCs. To further validate whether the luminescence occurred from the triplet state at room temperature, we compared the room-temperature and low-temperature time-resolved emission spectra. For that, time-resolved emission spectra are recorded at 300 K (time delay of 1.6 µs) and 77 K (time delay of 5 µs), shown in Figure **5b.** TRES at 300 K and 77 K show an overlap with the emergence of two peaks at low temperatures. The deconvoluted peaks for 77 K are shown in **Figure S8.** The spectral overlap at two different temperatures with a microsecond time delay signifies that the dominating pathway of emission in BSA-Au NCs is RTP. Further, no lower energy spectral shift at 77 K rules out the TADF process in BSA-Au NCs. The lifetime of BSA-Au NCs measured at 77 K comes out to be 18 µs (**Figure 5c**).

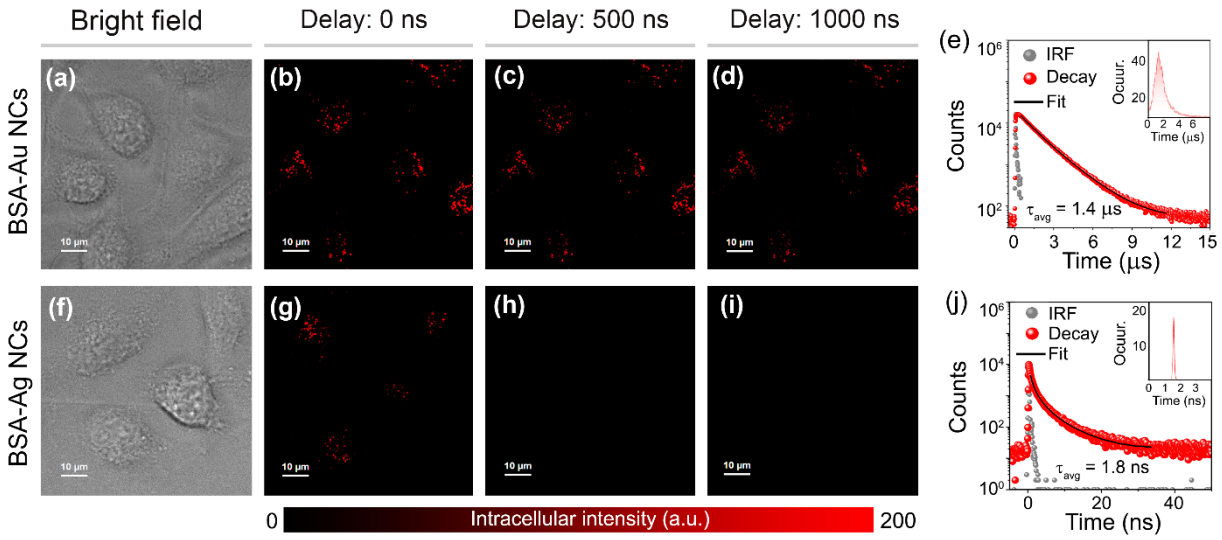

Figure 6: Time-resolved imaging of HeLa cells stained with an aqueous dispersion of (a-e) BSA-Au NCs (λ_{ex} = 470 nm, and λ_{em} = 488-800 nm) and (f-j) BSA-Ag NCs (λ_{ex} = 470 nm, and λ_{em} = 488-800 nm): (a, f) bright field images, (b, g) confocal laser scanning microscopy (CLSM) images with no time delay, time-gated images after a time delay of (c, h) 500 ns and (d, i) 1000 ns; scale = 10 μm. A common luminescence intensity scale is also indicated. Intracellular decay profile of (e) BSA-Au NCs and (j) BSA-Ag NCs incubated in HeLa cells (λ_{ex} = 470 nm, and λ_{em} = 488-800 nm, repetition rate = 50 kHz); inset: intracellular lifetime histograms are depicted.

The long-lived emission in BSA-MNCs prompts us to investigate the applicability of such probes in time-resolved luminescence imaging (TRLI).[46,47] The confocal laser scanning microscopy (CLSM) images of BSA-Au NCs (1 mg mL^{-1}) stained HeLa cells depicted bright red fluorescence signals from the cytoplasmic region of the cells (**Figure S9a, 6b**). Previous studies have shown that BSA-conjugated NCs are selectively transported to lysosomes.[38,48,49] Colocalization studies using LysoTracker™ Green (LTG) confirmed that BSA-Au NCs specifically localize into the lysosomes (**Figure S9b**). Next, we acquired TRLI images of BSA-Au NCs (1 mg mL^{-1}) stained HeLa cells by applying different delay times (**Figure 6a - 6e**). The corresponding time-gated images obtained from cells demonstrated noticeable luminescence even with a time delay of 1 μs (**Figure 6d, S10**). In contrast, upon applying a time delay of 1 μs, any noticeable luminescence was not observed from HeLa cells stained with BSA-Ag NCs (1 mg mL^{-1}), again suggesting its weak triplet harvesting nature under aqueous conditions (**Figure 6f - 6j, S10**).

In summary, we have shown the distinct excited state dynamics of BSA-Au NCs and BSA-Ag NCs. It is found that the deexcitation pathways were significantly influenced by charge transfer states formed via M-S bonds, the stability, and the rigidity of the protein coated nanoclusters. From TRES and TRANES analysis, we concluded that the emission in BSA-Ag NCs comes from the core states only, while BSA-Au NCs exhibits a dual emission consisting of short- and long-lived states, originating due to core and surface state interactions. Quenching studies with methyl viologen confirmed the presence of core and surface state interactions via LMCT states in BSA-Au NCs, leading to facile triplet harvesting at room temperature. In contrast, the BSA-Ag NCs exhibit fluorescence as the deexcitation mechanism at room temperature, transitioning to phosphorescence with sub-millisecond lifetimes under cryogenic conditions. Conversely, LMCT states in BSA-Au NCs facilitate triplet-state harvesting, resulting in RTP as the dominant mechanism with a microsecond lifetime. The time-resolved luminescence imaging of both MNCs in HeLa cells ascertained the long-lived emission characteristics in BSA-Au NCs but not in BSA-Ag NCs.

Author Contributions

S.S. conceptualized and designed all the experiments. S.S. and S.D. conducted various steady state and time-resolved luminescence measurements and analyzed the data with the help of C.K.N. and A.P. S.D. also performed time-resolved luminescence imaging for cell-related study. K.K. wrote the MATLAB code to automate the analysis of TRANES. C.K.N. and A.P. guided the complete project thoroughly and wrote the manuscript with the help of S.S. and S.D.

Acknowledgements

The authors thank the Advanced Material Research Centre (AMRC) of IIT Mandi and the Indian Institute of Science Education and Research Bhopal (IISERB), India, for providing the facilities and the sophisticated instruments. The financial support from the Indo-French Centre for the Promotion of Advanced Research (IFCPAR/CEFIPRA, Project No.: 6705-1) is gratefully acknowledged by A.P. C.K.N. thanks to SERB core research grant (CRG) India project number CRG/2020/000268 for the financial support. S.D. thanks, IISERB, for the fellowship. S.S. and K.K. thank the Ministry of Education, India (MoE), for research scholarships.

Supporting Information

Sections I, II and III providing the description of the materials and the synthesis procedures; **Instrumentation section (IV. a-j)** including brief explanation of the characterization methods, sample preparation, equations, and calculation parameters. **Supplementary section (V)** and **(VI)** containing figures and tables of material characterization, photophysical and intracellular studies.

References

(1) Buschmann, D. A.; Hirai, H.; Tsukuda, T. Tuning Photoluminescence Properties of Au Clusters by Surface Modification and Doping: Lessons from Case Studies of Icosahedral Au 13. *Inorg. Chem. Front.* **2024**, *11* (20), 6694–6710. https://doi.org/10.1039/D4QI01773K.

(2) Sharma, S.; Kaushik, K.; Salam, A.; Garg, R.; Mondal, J.; Lamba, R.; Kaur, M.; Nandi, C. K. Recent Advances in Long-Lived Emission in Coinage Metal Nanoclusters: Implications for Optoelectronic Applications. *ACS Appl. Nano Mater.* **2024**, *7* (1), 32–60. https://doi.org/10.1021/acsanm.3c04748.

(3) Lin, H.; Song, X.; Chai, O. J. H.; Yao, Q.; Yang, H.; Xie, J. Photoluminescent Characterization of Metal Nanoclusters: Basic Parameters, Methods, and Applications. *Adv. Mater.* **2024**, *36* (25), 1–22. https://doi.org/10.1002/adma.202401002.

(4) Zhou, M.; Jin, R. Optical Properties and Excited-State Dynamics of Atomically Precise Gold Nanoclusters. *Annu. Rev. Phys. Chem.* **2021**, *72* (1), 121–142. https://doi.org/10.1146/annurev-physchem-090419-104921.

(5) Xavier, P. L.; Chaudhari, K.; Baksi, A.; Pradeep, T. Protein-Protected Luminescent Noble Metal Quantum Clusters: An Emerging Trend in Atomic Cluster Nanoscience. *Nano Rev.* **2012**, *3* (1), 14767. https://doi.org/10.3402/nano.v3i0.14767.

(6) Chen, L.; Gharib, M.; Zeng, Y.; Roy, S.; Nandi, C. K.; Chakraborty, I. Advances in Bovine Serum Albumin-Protected Gold Nanoclusters: From Understanding the Formation Mechanisms to Biological Applications. *Mater. Today Chem.* **2023**, *29*, 101460. https://doi.org/10.1016/j.mtchem.2023.101460.

(7) Tan, S. C. L.; He, Z.; Wang, G.; Yu, Y.; Yang, L. Protein-Templated Metal Nanoclusters: Molecular-like Hybrids for Biosensing, Diagnostics and Pharmaceutics. *Molecules*. July 20, 2023, p 5531. https://doi.org/10.3390/molecules28145531.

(8) Chaudhari, K.; Xavier, P. L.; Pradeep, T. Understanding the Evolution of Luminescent Gold Quantum Clusters in Protein Templates. *ACS Nano* **2011**, *5* (11), 8816–8827. https://doi.org/10.1021/nn202901a.

(9) Zare, I.; Chevrier, D. M.; Cifuentes-Rius, A.; Moradi, N.; Xianyu, Y.; Ghosh, S.; Trapiella-Alfonso, L.; Tian, Y.; Shourangiz-Haghighi, A.; Mukherjee, S.; Fan, K.; Hamblin, M. R. Protein-Protected Metal Nanoclusters as Diagnostic and Therapeutic Platforms for Biomedical Applications. *Mater. Today* **2023**, *66*, 159–193. https://doi.org/10.1016/j.mattod.2020.10.027.

(10) Akyüz, E.; Şen, F. B.; Bener, M.; Başkan, K. S.; Tütem, E.; Apak, R. Protein-Protected Gold Nanocluster-Based Biosensor for Determining the Prooxidant Activity of Natural Antioxidant Compounds. *ACS Omega* **2019**, *4* (1), 2455–2462. https://doi.org/10.1021/acsomega.8b03286.

(11) Aires, A.; Fernández-Luna, V.; Fernández-Cestau, J.; Costa, R. D.; Cortajarena, A. L. White-Emitting Protein-Metal Nanocluster Phosphors for Highly Performing Biohybrid Light-Emitting Diodes. *Nano Lett.* **2020**, *20* (4), 2710–2716. https://doi.org/10.1021/acs.nanolett.0c00324.

(12) Yang, T.-Q.; Peng, B.; Shan, B.-Q.; Zong, Y.-X.; Jiang, J.-G.; Wu, P.; Zhang, K. Origin of the Photoluminescence of Metal Nanoclusters: From Metal-Centered Emission to

Ligand-Centered Emission. *Nanomaterials* **2020**, *10* (2), 261. https://doi.org/10.3390/nano10020261.

(13) Kang, X.; Zhu, M. Tailoring the Photoluminescence of Atomically Precise Nanoclusters. *Chem. Soc. Rev.* **2019**, *48* (8), 2422–2457. https://doi.org/10.1039/c8cs00800k.

(14) Yao, Q.; Wu, Z.; Liu, Z.; Lin, Y.; Yuan, X.; Xie, J. Molecular Reactivity of Thiolate-Protected Noble Metal Nanoclusters: Synthesis, Self-Assembly, and Applications. *Chem. Sci.* **2021**, *12* (1), 99–127. https://doi.org/10.1039/d0sc04620e.

(15) Zare, I.; Chevrier, D. M.; Cifuentes-Rius, A.; Moradi, N.; Xianyu, Y.; Ghosh, S.; Trapiella-Alfonso, L.; Tian, Y.; Shourangiz-Haghighi, A.; Mukherjee, S.; Fan, K.; Hamblin, M. R. Protein-Protected Metal Nanoclusters as Diagnostic and Therapeutic Platforms for Biomedical Applications. *Mater. Today* **2023**, *66*, 159–193. https://doi.org/10.1016/j.mattod.2020.10.027.

(16) Yan, L.; Cai, Y.; Zheng, B.; Yuan, H.; Guo, Y.; Xiao, D.; Choi, M. M. F. Microwave-Assisted Synthesis of BSA-Stabilized and HSA-Protected Gold Nanoclusters with Red Emission. *J. Mater. Chem.* **2012**, *22* (3), 1000–1005. https://doi.org/10.1039/c1jm13457d.

(17) Meng, X.; Zare, I.; Yan, X.; Fan, K. Protein-Protected Metal Nanoclusters: An Emerging Ultra-Small Nanozyme. *WIREs Nanomedicine and Nanobiotechnology* **2020**, *12* (3), e1602. https://doi.org/10.1002/wnan.1602.

(18) Zhang, W.; Ye, J.; Zhang, Y.; Li, Q.; Dong, X.; Jiang, H.; Wang, X. One-Step Facile Synthesis of Fluorescent Gold Nanoclusters for Rapid Bio-Imaging of Cancer Cells and Small Animals. *RSC Adv.* **2015**, *5* (78), 63821–63826. https://doi.org/10.1039/c5ra11321k.

(19) Guan, R.; Tao, L.; Hu, Y.; Zhang, C.; Wang, Y.; Hong, M.; Yue, Q. Selective Determination of Ag+in the Presence of Cd2+, Hg2+and Cu2+based on Their Different Interactions with Gold Nanoclusters. *RSC Adv.* **2020**, *10* (55), 33299–33306. https://doi.org/10.1039/d0ra05787h.

(20) Zhou, W.; Cao, Y.; Sui, D.; Guan, W.; Lu, C.; Xie, J. Ultrastable BSA-Capped Gold Nanoclusters with a Polymer-like Shielding Layer against Reactive Oxygen Species in Living Cells. *Nanoscale* **2016**, *8* (18), 9614–9620. https://doi.org/10.1039/c6nr02178f.

(21) Basu, N.; Mandal, D. Time-Dependent Emission Stokes Shift in Au, Ag and Au/Ag Fluorescent Nanoclusters: Evidence of Multiple Emissive States. *Photochem. Photobiol. Sci.* **2019**, *18* (7), 1782–1792. https://doi.org/10.1039/c8pp00540k.

(22) Shi, J.; Cooper, J. K.; Lindley, S.; Williams, O.; Kliger, D. S.; Xu, Y.; Bao, Y.; Zhang, J. Z. The Excited State Dynamics of Protein-Encapsulated Au Nanoclusters. *Chem. Phys. Lett.* **2014**, *610–611*, 125–130. https://doi.org/10.1016/j.cplett.2014.07.009.

(23) Stamplecoskie, K. G.; Kamat, P. V. Size-Dependent Excited State Behavior of Glutathione-Capped Gold Clusters and Their Light-Harvesting Capacity. *J. Am. Chem. Soc.* **2014**, *136* (31), 11093–11099. https://doi.org/10.1021/ja505361n.

(24) Agrawal, S.; Shil, D.; Gupta, A.; Mukherjee, S. Superstructures of Copper Nanoclusters as NIR TADF Emitters: Solvent-Dependent Optical and Morphological Modulation. *Nanoscale* **2024**, *16* (44), 20556–20569. https://doi.org/10.1039/D4NR03074E.

(25) Lin, H. T.; Cai, K. B.; Huang, H. Y.; Lin, T. N.; Shen, J. L.; Lin, C. A. J.; Yuan, C. T. Thermally-Activated Delayed Fluorescence from Biocompatible, Solid-State Gold Nanoclusters Embedded into Ionic-Crystal Matrices. *J. Lumin.* **2017**, *187*, 269–273. https://doi.org/10.1016/j.jlumin.2017.03.032.

(26) Liu, Z.; Luo, L.; Kong, J.; Kahng, E.; Zhou, M.; Jin, R. Bright Near-Infrared Emission from the Au39(SR)29 Nanocluster. *Nanoscale* **2024**, *16* (15), 7419–7426. https://doi.org/10.1039/d4nr00677a.

(27) Li, Q.; Zhou, M.; So, W. Y.; Huang, J.; Li, M.; Kauffman, D. R.; Cotlet, M.; Higaki, T.; Peteanu, L. A.; Shao, Z.; Jin, R. A Mono-Cuboctahedral Series of Gold Nanoclusters: Photoluminescence Origin, Large Enhancement, Wide Tunability, and Structure-Property Correlation. *J. Am. Chem. Soc.* **2019**, *141* (13), 5314–5325. https://doi.org/10.1021/jacs.8b13558.

(28) Stamplecoskie, K. G.; Chen, Y. S.; Kamat, P. V. Excited-State Behavior of Luminescent Glutathione-Protected Gold Clusters. *J. Phys. Chem. C* **2014**, *118* (2), 1370–1376. https://doi.org/10.1021/jp410856h.

(29) Bhattacharjee, I.; Acharya, N.; Bhatia, H.; Ray, D. Dual Emission through Thermally Activated Delayed Fluorescence and Room-Temperature Phosphorescence, and Their Thermal Enhancement via Solid-State Structural Change in a Carbazole-Quinoline Conjugate. *J. Phys. Chem. Lett.* **2018**, *9* (11), 2733–2738. https://doi.org/10.1021/acs.jpclett.8b00937.

(30) Monkman, A. Photophysics of Thermally Activated Delayed Fluorescence. In *Highly Efficient OLEDs*; Wiley, 2018; pp 425–463. https://doi.org/10.1002/9783527691722.ch12.

(31) Xie, J.; Zheng, Y.; Ying, J. Y. Protein-Directed Synthesis of Highly Fluorescent Gold Nanoclusters. *J. Am. Chem. Soc.* **2009**, *131* (3), 888–889. https://doi.org/10.1021/ja806804u.

(32) Chen, Y.; Feng, T.; Chen, L.; Gao, Y.; Di, J. Bovine Serum Albumin Stabilized Silver Nanoclusters as "Signal-on" Fluorescent Probe for Detection of Hydrogen Peroxide and Glucose. *Opt. Mater. (Amst).* **2021**, *114* (February), 111012. https://doi.org/10.1016/j.optmat.2021.111012.

(33) Wen, X.; Yu, P.; Toh, Y. R.; Tang, J. Structure-Correlated Dual Fluorescent Bands in BSA-Protected Au 25 Nanoclusters. *J. Phys. Chem. C* **2012**, *116* (21), 11830–11836. https://doi.org/10.1021/jp303530h.

(34) Raut, S.; Chib, R.; Rich, R.; Shumilov, D.; Gryczynski, Z.; Gryczynski, I. Polarization Properties of Fluorescent BSA Protected Au25 Nanoclusters. *Nanoscale* **2013**, *5* (8), 3441–3446. https://doi.org/10.1039/c3nr34152f.

(35) Bolli, E.; Mezzi, A.; Burratti, L.; Prosposito, P.; Casciardi, S.; Kaciulis, S. X-Ray and UV Photoelectron Spectroscopy of Ag Nanoclusters. *Surf. Interface Anal.* **2020**, *52* (12), 1017–1022. https://doi.org/10.1002/sia.6783.

(36) Porcaro, F.; Carlini, L.; Ugolini, A.; Visaggio, D.; Visca, P.; Fratoddi, I.; Venditti, I.; Meneghini, C.; Simonelli, L.; Marini, C.; Olszewski, W.; Ramanan, N.; Luisetto, I.; Battocchio, C. Synthesis and Structural Characterization of Silver Nanoparticles Stabilized with 3-Mercapto-1-Propansulfonate and 1-Thioglucose Mixed Thiols for Antibacterial Applications. *Materials (Basel).* **2016**, *9* (12), 1028.

https://doi.org/10.3390/ma9121028.

(37) Castner, D. G.; Hinds, K.; Grainger, D. W. X-Ray Photoelectron Spectroscopy Sulfur 2p Study of Organic Thiol and Disulfide Binding Interactions with Gold Surfaces. *Langmuir* **1996**, *12* (21), 5083–5086. https://doi.org/10.1021/la960465w.

(38) Yadav, A.; Verma, N. C.; Rao, C.; Mishra, P. M.; Jaiswal, A.; Nandi, C. K. Bovine Serum Albumin-Conjugated Red Emissive Gold Nanocluster as a Fluorescent Nanoprobe for Super-Resolution Microscopy. *J. Phys. Chem. Lett.* **2020**, *11* (14), 5741–5748. https://doi.org/10.1021/acs.jpclett.0c01354.

(39) Paul, S.; Sepay, N.; Sarkar, S.; Roy, P.; Dasgupta, S.; Saha Sardar, P.; Majhi, A. Interaction of Serum Albumins with Fluorescent Ligand 4-Azido Coumarin: Spectroscopic Analysis and Molecular Docking Studies. *New J. Chem.* **2017**, *41* (24), 15392–15404. https://doi.org/10.1039/c7nj02335a.

(40) Baral, A.; Satish, L.; Das, D. P.; Sahoo, H.; Ghosh, M. K. Construing the Interactions between MnO2 Nanoparticle and Bovine Serum Albumin: Insight into the Structure and Stability of a Protein-Nanoparticle Complex. *New J. Chem.* **2017**, *41* (16), 8130–8139. https://doi.org/10.1039/c7nj01227f.

(41) Qiu, K.; Yadav, A.; Tian, Z.; Guo, Z.; Shi, D.; Nandi, C. K.; Diao, J. Ultralong-Term Super-Resolution Tracking of Lysosomes in Brain Organoids by Near-Infrared Noble Metal Nanoclusters. *ACS Mater. Lett.* **2022**, *4* (9), 1565–1573. https://doi.org/10.1021/acsmaterialslett.2c00436.

(42) Sharma, S.; Das, S.; Kaushik, K.; Yadav, A.; Patra, A.; Nandi, C. K. Unveiling the Long-Lived Emission of Copper Nanoclusters Embedded in a Protein Scaffold. *J. Phys. Chem. Lett.* **2023**, *14* (40), 8979–8987. https://doi.org/10.1021/acs.jpclett.3c01877.

(43) Periasamy, N. *Chapter 2 Heterogeneity of Fluorescence Determined by the Method of Area-Normalized Time-Resolved Emission Spectroscopy*, 1st ed.; Elsevier Inc., 2008; Vol. 450. https://doi.org/10.1016/S0076-6879(08)03402-2.

(44) Devadas, M. S.; Kim, J.; Sinn, E.; Lee, D.; Goodson, T.; Ramakrishna, G. Unique Ultrafast Visible Luminescence in Monolayer-Protected Au 25 Clusters . *J. Phys. Chem. C* **2010**, *114* (51), 22417–22423. https://doi.org/10.1021/jp107033n.

(45) Khan, S.; Verma, N. C.; Gupta, A.; Nandi, C. K. Reversible Photoswitching of Carbon Dots. *Sci. Rep.* **2015**, *5* (1), 11423. https://doi.org/10.1038/srep11423.

(46) V T K, S.; Das, S.; Patra, A. Endoplasmic Reticulum-Targeting Delayed Fluorescent Probe for Dual-mode Nitroreductase Sensing. *Chem. – An Asian J.* **2024**, e202401226. https://doi.org/10.1002/asia.202401226.

(47) Das, S.; Batra, A.; Kundu, S.; Sharma, R.; Patra, A. Unveiling Autophagy and Aging through Time-Resolved Imaging of Lysosomal Polarity with a Delayed Fluorescent Emitter. *Chem. Sci.* **2023**, *15* (1), 102–112. https://doi.org/10.1039/d3sc02450d.

(48) Marwaha, R.; Sharma, M. DQ-Red BSA Trafficking Assay in Cultured Cells to Assess Cargo Delivery to Lysosomes. *Bio-protocol* **2017**, *7* (19), e2571. https://doi.org/10.21769/BioProtoc.2571.

(49) Yadav, A.; Kaushik, K.; Sharma, S.; Anjum, F.; Nandi, C. K. Near-Infrared-Emitting Silver Nanoclusters as Fluorescent Probes for Super-Resolution Radial Fluctuation Imaging of Lysosomes. *ACS Appl. Nano Mater.* **2022**, *5* (7), 9260–9265.

https://doi.org/10.1021/acsanm.2c01604.

Graphical Abstract-Table of Content

Revisiting Protein Protected Gold and Silver Nanoclusters: Excited State Dynamics and Long-Lived Emission

Shagun Sharma[a], Subhadeep Das[b], Kush Kaushik[a], Abhijit Patra[b] Chayan Kanti Nandi[a]*

[a]School of Chemical Sciences, Indian Institute of Technology (IIT) Mandi, H.P- 175075

[b]Department of Chemistry, Indian Institute of Science Education and Research (IISER) Bhopal, M.P-462066

Email: *chayan@iitmandi.ac.in*

abhijit@iiserb.ac.in

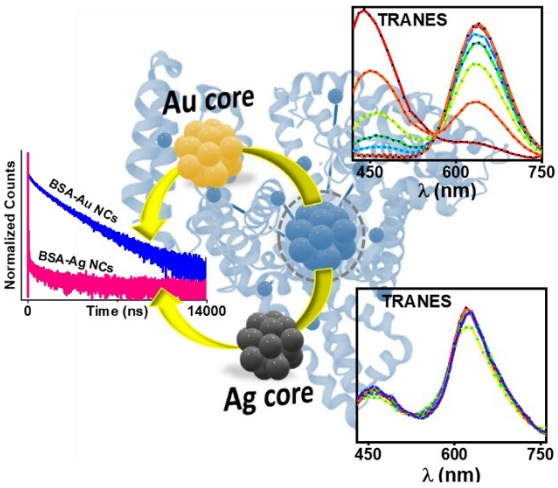

Time-Resolved Luminescence Insights into the Distinct Excited State Dynamics of Protein-Conjugated Gold and Silver Nanoclusters.